Bushiri, MJ.; Gopi, DN.; Monteseguro, V.; Sans-Tresserras, JÁ. (2021). High-pressure Raman investigation of high index facets bounded alpha-Fe2O3 pseudocubic crystals. Journal of Physics Condensed Matter. 33(8):1-10. https://doi.org/10.1088/1361-648X/abcb11

HIGH-PRESSURE RAMAN INVESTIGATION OF HIGH INDEX FACETS BOUNDED α-Fe_2O_3 PSEUDOCUBIC CRYSTALS

M. Junaid Bushiri[a,*], Divya Neravathu Gopi[a], Virginia Monteseguro[b, c] and Juan Angel Sans[d,*]

[a]Department of Physics, Cochin University of Science and Technology, Kochi-682022, Kerala, India

[b]Departamento Física Aplicada-ICMUV, Universidad de Valencia, MALTA Consolider Team, 46100 València, Spain

[c]DCITIMAC, Universidad de Cantabria, Avenida de los Castros 48, 39005 Santander, Spain

[d]Instituto de Diseño para la Fabricación y Producción Automatizada, Universitat Politècnica de València, MALTA Consolider Team, 46022 València, Spain

*Corresponding authors: junaidbushiri@gmail.com, juasant2@upv.es

Abstract

High index facet bounded α-Fe_2O_3 pseudocubic crystals has gained the attention of the scientific community due to its promising electrochemical sensing response towards aqueous ammonia. The structural stability of α-Fe_2O_3 pseudocubic crystals is investigated through high-pressure Raman spectroscopy up to 22.2 GPa, and whose results are compared with our *ab-initio* theoretical calculations. The symmetry of the experimental Raman-active modes has been assigned by comparison with theoretical data. In addition to the Raman-active modes, two additional Raman features are also detected, whose intensity increases with compression. The origin of these two additional peaks are addressed in this study, revealing a strong dependence on the geometry and the low dimensionality as the most plausible explanation.

Keywords: Iron oxide, alpha-Fe_2O_3, high pressure, Raman spectroscopy, α-Fe_2O_3 pseudocubic crystals.

Introduction

Iron (III) oxide exists in five different polymorphic forms such as α-Fe_2O_3 (hematite), β-Fe_2O_3, γ-Fe_2O_3 (maghemite), ε-Fe_2O_3, and ζ-Fe_2O_3, a recently discovered monoclinic structure [1,2]. Among these different polymorphic forms of iron oxide, hematite is the most common phase which exists in corundum structure at ambient conditions. Hematite is particularly useful for applications in the fields of catalysis, sensing, photoelectrochemical cells, magnetic resonance imaging, lithium-ion batteries, biomedical applications, etc. [3–9]. The growth of hematite nanomaterials (α-Fe_2O_3) with different sizes and shapes has gained intense research interest due to their unique chemical, physical, optical, magnetic, and electrochemical properties compared to its bulk counterparts [4–8,10]. Moreover, low dimensionality and geometry are major factors that influence the stability and properties of iron sesquioxides. For instance, the ε-phase of iron oxide is only stable at the nanocrystalline form that reveals its paramount mechanical stability under compression[11]. The hydrothermal synthesis is one of the most commonly employed synthesis processes for the growth of α-Fe_2O_3 nanoparticles, which usually produces spherical particles. Interestingly, the synthesis parameters such

as the nature of solvents, temperature, duration of reaction, pH, presence of additives, etc. play a pivotal role in determining the size, shapes, and morphologies of α-Fe_2O_3 grown by hydrothermal process [12–17]. However, nanomaterials with exposed high-index facets, in which a minimum of one Miller index representing the exposed facets being greater than unity (h, k, or l> 1), likely to show enhanced reaction efficiencies due to its peculiar surface properties. The morphology, size, and nature of exposed crystallographic facets of nanoparticles can produce equal impacts on their intrinsic properties and hence determine their applications. However, the high energy surfaces are usually being exposed only during the initial stages of crystal growth and vanish gradually towards the completion of the growth process under normal circumstances[18,19]. Metal ions can be used for the morphology induced growth of α-Fe_2O_3 with selective facets exposed. The presence of certain metal ions in the crystal growth medium under specific experimental conditions favors the exposure of selective facets on the surface of the as-grown crystals[18,20–23]. The growth of α-Fe_2O_3 pseudocubic crystals with exposed, electrochemically active, high index facets, {012}, $\{01\bar{4}\}$, and $\{\bar{2}10\}$ induced by employing Zn^{2+} metal ions as the structure inducing additive is reported by our group recently[24]. This material possesses low impedance, enhanced electrochemical properties, and promising electrochemical sensing efficiencies towards aqueous ammonia compared to spherical α-Fe_2O_3 nanoparticles synthesized in the absence of structure inducing Zn^{2+} additives[24]. As stated previously, the technological applications of electrochemically active, high-index facets bounded α-Fe_2O_3 pseudocubic crystals requires to carry out an extensive high-pressure (HP) structural investigations to understand the probable structural changes occur to these pseudocubic crystals under stress. The high-pressure analysis also enables us to investigate the capability of this material to host different dopants to tune its electrochemical properties.

The HP Raman scattering measurements of bulk α-Fe_2O_3 were reported by Shim et al up to an applied pressure of 54 GPa in which the Raman bands show a positive pressure dependence with a nonlinear pressure-induced shift[25]. The experimental and theoretical investigations on the pressure-induced structural phase transitions of α-Fe_2O_3 nanoparticles were previously reported from a shock-wave experiment carried out up to a pressure of 50 GPa[26]. The structural phase transition of powdered synthetic iron oxide (α-Fe_2O_3) was also investigated by Ono et al, up to 70 GPa pressure and temperatures above 2500 K, and observed a phase transition from corundum α-Fe_2O_3 to an orthorhombic perovskite-type Fe_2O_3 at about 30 GPa pressure, along with the formation of a new high-pressure phase of α-Fe_2O_3 above 50 GPa[27]. However, to the best of our knowledge, no experimental or theoretical attempts have ever been made to investigate the structural transitions that may occur in high index facets bounded α-Fe_2O_3 pseudocubic crystals. For α-Fe_2O_3, a reconstructive phase transition is expected from corundum to orthorhombic structure under HP[25]. Hence, the investigation of HP Raman spectroscopy of α-Fe_2O_3 pseudocubic crystals can shed light on the probable HP structural phase transition of high index faceted pseudocubic crystals. Thus, in the present work, the HP Raman spectra of high index faceted α-Fe_2O_3 pseudocubic crystals are investigated up

to 22.2 GPa. Moreover, the phonon frequency shifts and Grünesien parameters are compared with *ab initio* theoretical simulations.

Experimental description

The high index facets bounded α-Fe_2O_3 pseudocubic crystals investigated in the present work were grown by a solvo-hydrothermal process using Zn^{2+} metal ions as the structure inducing additive[24]. As reported previously, the various analyses such as XPS, EDX, etc. carried out on this sample had shown the presence of traces of Zn^{2+} ions on the surface of the pseudocubic crystals even though the XRD pattern had shown the formation of pure α-Fe_2O_3. Thus, the Rietveld Refinement was performed on the XRD pattern of the sample collected using the Bruker D8 Advance X-ray diffractometer (Cu K_α). The quantitative and qualitative phase analysis was performed with the Rietveld refinement method by using TOPAS 6.0 software to rule out the presence of other oxide phases in the sample.

The pressure-dependent Raman scattering measurements of the high index facets bounded α-Fe_2O_3 pseudocubic crystals were carried out using a confocal HORIBA Jobin-Yvon Lab Ram spectrometer equipped with a diffraction grating (1200 grooves mm^{-1}). For HP measurements, the sample was kept in a membrane-type diamond anvil cell (MDAC) using methanol-ethanol-water (16:3:1) mixture as the pressure transmitting medium. The pressure inside the cell was measured by monitoring the pressure-dependent fluorescence shift of ruby microspheres loaded besides the sample under investigation. After the compression of the sample loaded in the cell to the desired pressure, the Raman spectra were recorded under different applied pressure up to 22.2 GPa with a resolution better than 2 cm^{-1}.

Theoretical details

The density functional theory (DFT) formalism was used for a*b initio* calculations[28] with the VASP package to carry out the calculations with a projector augmented wave scheme (PAW)[29]. Highly converged results were obtained by extending the set of plane waves up to a kinetic energy cut-off of 550 eV. The calculations were performed using GGA + U formalism with Dudarev's approach for giving a reliable description of the effects of electronic correlation[30]. In order to get reliable results for the magnetic moments and the cell parameters as compared with the experimental data, the effective on-site Coulomb and exchange parameters were set to U = 4 eV and J = 1 eV respectively. A dense grid of k-special points was used to perform the integrations along the Brillouin zone (BZ).

The structures were fully relaxed to their equilibrium configuration through the calculation of forces on the atoms and the stress tensor at each selected volume. For the relaxed configurations, the forces on the atoms are found to be less than 0.006 eV/Å and the deviations of the stress tensor from a diagonal hydrostatic form are estimated as less than 0.1 GPa. Similar to the total energy E(V) and the theoretical pressure P(V) in

function of the volume, can be obtained with the DFT method. The theoretical pressure P, just as the other derivatives of energy, is obtained from the calculated stress[31]. The lattice-dynamic calculations were performed at the zone center (Γ point) of the Brillouin Zone (BZ). Highly converged results on the forces are essential for the calculation of dynamical matrix using the direct force constant approach[32,33]. The dynamical matrix at the Γ point of the BZ was constructed with separate calculations of forces by considering the fixed displacement of atoms from their equilibrium configuration within the primitive cell. The number of such independent displacements in the analyzed structures is found to be reduced which can be ascribed to the crystal symmetry of α-Fe_2O_3 pseudocubic crystals. The frequencies of the normal modes were obtained by the diagonalization of the dynamical matrix. The symmetry and eigenvectors of the vibrational modes at the Γ point in each structure were also obtained based on these calculations.

Results and discussion

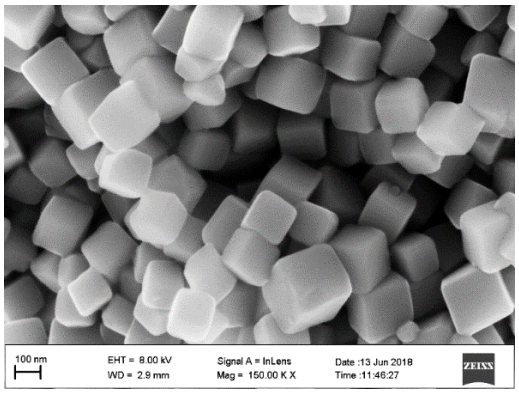

Figure 1: Field Emission Scanning Electron Microscopy (FESEM) image of high index facets bounded α-Fe_2O_3 pseudocubic crystals synthesized in the presence of Zn^{2+} ions as a structure inducing additive by solvo-hydrothermal process.

The morphological features of the pseudocubic α-Fe_2O_3 crystals with exposed high index facets {012}, $\{01\bar{4}\}$, and $\{\bar{2}10\}$ used in the present investigation, are identified with FESEM. These crystals are having an average edge length of 120 nm with a dihedral angle of 85° as reported[24]. A representative FESEM image of the α-Fe_2O_3 pseudocubic crystals is shown in Figure 1.

The XRD pattern of the grown crystals matches with the JCPDS card no. 80-2377 and all the Braggs diffraction peaks of α-Fe_2O_3 pseudocubic crystals could be indexed to α-Fe_2O_3 as reported[24]. The Hematite (α-Fe_2O_3) adopts a corundum structure at ambient conditions which crystallize in the hexagonal crystal system with two independent crystallographic sites, one for Fe and another for O atoms with a space group $R\bar{3}c$ [1]. Each iron atoms of α-Fe_2O_3 are bonded by six oxygen atoms with varying bond lengths, forming several distorted octahedrons.

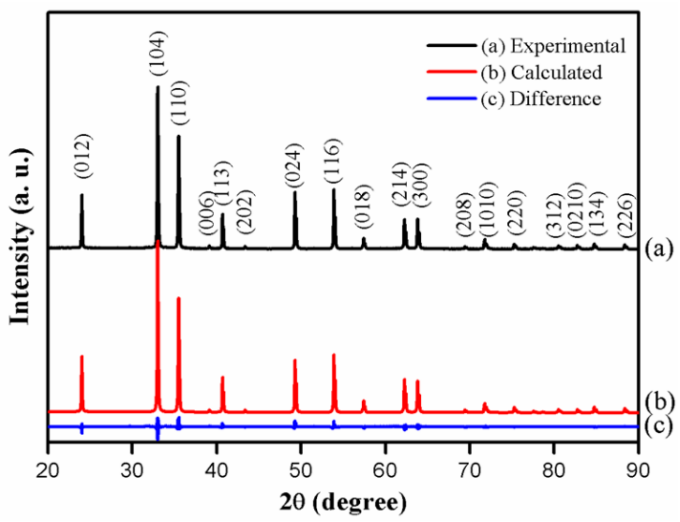

Figure 2: Rietveld refinement carried out on the XRD pattern of high index facets bounded α-Fe_2O_3 pseudocubic crystals, synthesized in the presence of Zn^{2+} ions as a structure inducing additive by solvo-hydrothermal method, (a) experimental, (b) calculated XRD data, and (c) difference pattern between the experimental and calculated data.

Phase	Hematite (100%)
Bragg R-factor	2.067
Space Group	$R\bar{3}c$
Cell Mass	949.573
Cell Volume ($Å^3$)	302.6320
Strain L	0.0333
Crystal Density (g/cm^3)	5.210
Lattice Parameters (Å)	a=5.0390, c =13.7620

Table 1: Rietveld refinement analysis results of high index facets bounded α-Fe_2O_3 pseudocubic crystals, synthesized in the presence of Zn^{2+} ions as a structure inducing additive by solvo-hydrothermal method.

In order to know the exact phase of the synthesized iron oxide sample, Rietveld refinement of the powder XRD data[34] is carried out by employing TOPAS version 6.0 software, and the results of which are given in Figure 2. This study reveals that the sample under investigation is α-Fe_2O_3, and the obtained structural parameters agree with the International Crystal Structure Database (ICSD 182840). The blue curve at the bottom of Figure 2 represents the difference between the simulated and experimental XRD patterns, with a goodness of fit (S) around 1.88[35]. The structural parameters obtained from the refinement analysis are summarized in Table 1. There is a good agreement between the experimental and simulated XRD patterns that indicates the single-phase formation of α-Fe_2O_3 in the hexagonal crystal system (space group: $R\bar{3}c$). The room temperature lattice constants of α-Fe_2O_3 pseudocubic crystals are calculated as a = 5.039 Å and c = 13.762 Å with error percentages of 0.019 % and 0.07 % respectively, which is in comparison with the standard lattice constants (a = 5.038 Å, c = 13.772 Å) of α-Fe_2O_3. The unit cell structural model of the sample under investigation based on the data derived from the Rietveld refinement analysis is shown in Figure 3.

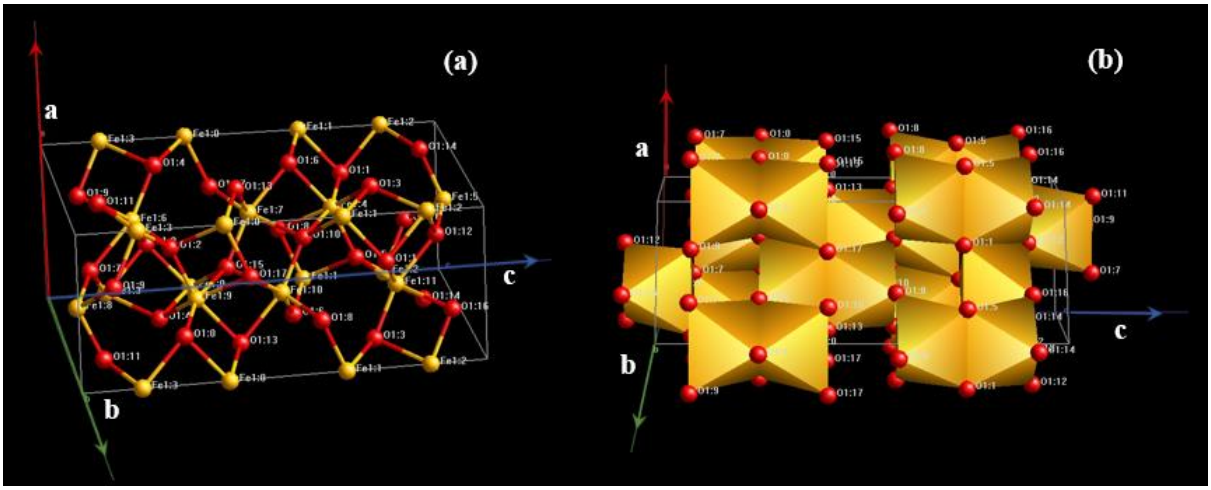

Figure 3: (a) Unit cell representation of high index facets bounded α-Fe_2O_3 pseudocubic crystals, synthesised in the presence of Zn^{2+} ion as a structure inducing additive by solvo-hydrothermal method, (b) face-sharing octahedra of α-Fe_2O_3 pseudocubic crystals (Colour scheme: Fe = yellow, and O = red).

The group theory predicts that the hematite with D_{3d}^6 group symmetry has the following vibrational modes in the Raman spectrum at the zone-centre[36,37],

$$\Gamma_{vib} = 2A_{1g} + 2A_{1u} + 3A_{2g} + 2A_{2u} + 5E_g + 4E_u \quad (1)$$

Among these, $1A_{2u}$ and $1E_u$ are the acoustic modes, the $2A_{1g}+5E_g$ modes are Raman-active. The $2A_{2u}+4E_u$ modes are infrared-active, whereas $2A_{1u}+3A_{2g}$ modes are inactive both in Raman and IR[25,38]. The vibrations involved in each Raman-active modes in a primitive cell of α-Fe_2O_3 obtained by theoretical simulations is shown in Figure 4, in which the brown and blue spheres correspond to iron and oxygen atoms of α-Fe_2O_3 respectively.

The preliminary analysis of the Raman spectrum of high index facets bounded α-Fe_2O_3 pseudocubic crystals at ambient pressure (Figure 5) allows the identification of seven Raman-active modes predicted by the group theory together with two additional Raman features. Additionally, the presence of any impurity phases in the as-synthesized α-Fe_2O_3 pseudocubic crystals due to the availability of Zn^{2+} ions in the precursor solution is not identified from the Raman spectra within the detection limit of the technique. In the present work, we could follow the HP behavior of all the seven Raman-active modes ($2A1g$ and $5Eg$) plus that of the two additional modes (likely to be infrared active modes). The two additional Raman bands (minor bands around 381 and 661 cm^{-1}) marked with two small asterisks in the Raman spectra of α-Fe_2O_3 pseudocubic crystals at 1 atm are not associated with the presence of any impurities. The origin of these Raman bands in the spectra of α-Fe_2O_3 pseudocubic crystals will be discussed later.

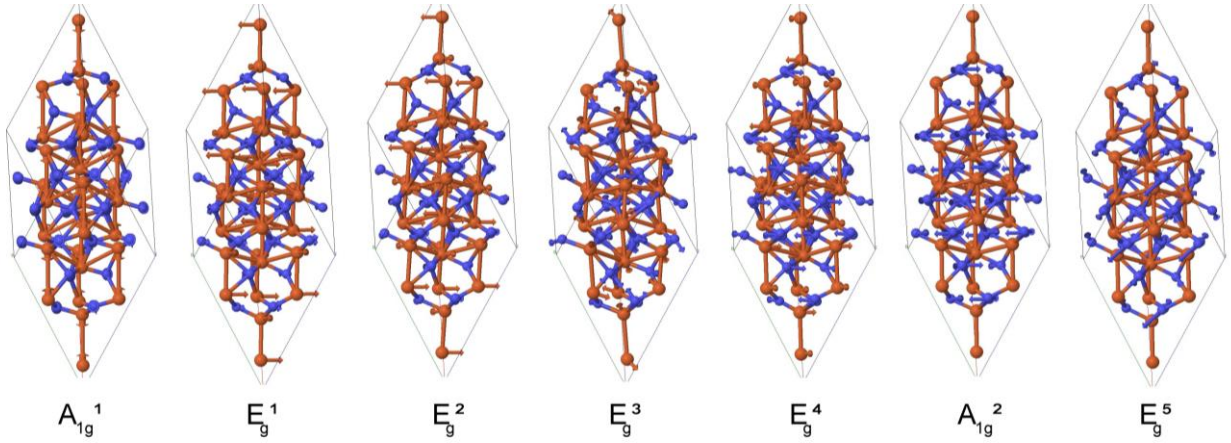

Figure 4: Representation of vibrations involved in each Raman-active modes in a primitive cell of α-Fe_2O_3 obtained from theoretical simulations. Brown and blue spheres correspond to the iron and oxygen atoms of α-Fe_2O_3 respectively.

A detailed analysis of the vibrations of Raman-active modes (Figure 4) revealed that the low-frequency modes are more prominently dominated by the movement of iron atoms (with higher mass) than the high-frequency modes, which are mainly associated with the vibrations of oxygen atoms (with lower mass). Thus the lowest frequency mode with A_{1g}^{1} symmetry is observed experimentally (theoretically) around 225 cm^{-1} (205 cm^{-1}) at ambient pressure which only involves the movement of iron atoms, whereas the oxygen atoms remain insensitive to these vibrations. In this case, the iron atoms oscillate with bending characteristics compared to the iron atoms in the same crystallographic plane. That is similar to scissoring oscillational motions but with stretching characteristics compared to iron atoms of neighboring crystallographic planes. The E_g^{1} mode shows an experimental (theoretical) frequency at ambient conditions around 244 (213) cm^{-1}, which is related to the typical bending vibrations of iron atoms with respect to oxygen atoms, where the bottom half of the iron atoms along the a-axis of the primitive cell vibrates in-phase and counter phase with those on the top half of primitive cell. The E_g^{2} mode is associated with a stretching mode of vibrations with an experimental (theoretical) frequency at ambient conditions around 290 (268) cm^{-1}, whose atoms are vibrating transversally to the a-axis and the oxygen atoms begin to participate in these vibrations. In E_g^{3} mode, whose experimental (theoretical) frequency at ambient conditions shows a value around 296 (275) cm^{-1}, which can be considered as an asymmetric stretching mode of vibrations of oxygen atoms. On the other hand, the vibrations of E_g^{4} mode, with an experimental (theoretical) frequency at room conditions around 409 (371) cm^{-1}, shows the participation of both iron and oxygen atoms in a mix between stretching and bending characteristics. However, in the mode A_{1g}^{2}, oxygen atoms have a counter phase twisting movement with an experimental (theoretical) frequency around 499 (448) cm^{-1}. The highest frequency mode, E_g^{5} with an experimental (theoretical) frequency around 611 (578) cm^{-1} shows the stretching mode of vibrations of oxygen atoms along Fe-O interatomic distance. Thus, the highest frequency mode is the vibration of the lightest atom (lowest mass) along with the shortest interatomic distance, which increases the oscillator strength or the spring constant of vibrations.

Symmentry Raman-active modes	Vibrations involved
A_{1g}^{1}	Movement of iron atoms only, oxygen atoms remain insensitive to these vibrations
E_g^{1}	Bending vibration of the iron atoms around the oxygen atoms
E_g^{2}	Atoms are vibrating transversally to a-axis and oxygen atoms
E_g^{3}	Asymmetric stretching mode of vibrations of oxygen atoms
E_g^{4}	Participation of both iron and oxygen atoms in a mix between stretching and bending characteristics
A_{1g}^{2}	Oxygen atoms have a counter phase twisting movement
E_g^{5}	Stretching mode of vibrations of oxygen atoms along Fe-O interatomic distance

Table 2: Origin of vibrations involved in different Raman modes of in a primitive cell of α-Fe_2O_3 obtained from theoretical simulations.

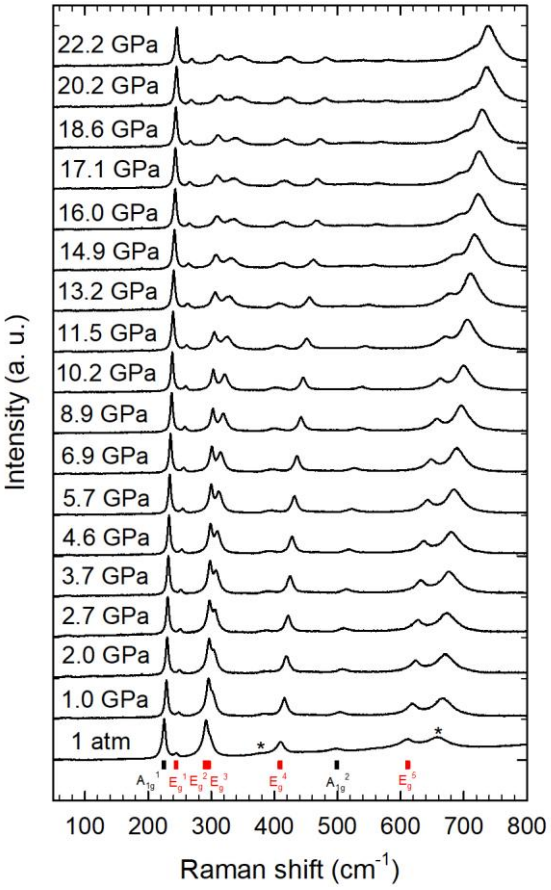

Figure 5: Raman spectra of high index facets bounded α-Fe_2O_3 pseudocubic crystals, synthesised in the presence of Zn^{2+} ions as a structure inducing additive by solvo-hydrothermal method in the pressure range of 1-22.2 GPa. The two unexpected Raman features are indicated by asterisks.

The HP dependence of Raman scattering spectra shows a monotonous shift in the Raman features towards the higher frequency upon compression (Figure 6). The dependence of all the seven Raman-active modes ($2A_{1g}$ and $5E_g$) plus that of the two additional modes (likely to be infrared active modes) on pressure showed a nice agreement with the theoretical simulations as displayed in Figure 6, with a classical underestimation of the theoretically simulated frequency. To analyze the evolution of the two additional Raman features observed, linear fits to these Raman modes are further investigated. The literature reported a classical sublinear behavior of the HP dependence of the Raman frequencies under pressure up to 62 GPa [25]. However, in the present case, the measurements were performed only up to 22 GPa applied pressure, which belongs to the linear region of the reported HP dependence. The comparison of our results with the Raman studies of bulk hematite under compression showed similar frequencies for the Raman-active modes at ambient pressure (Table 4). The pressure dependence of all phonon modes of α-Fe_2O_3 pseudocubic crystals is also analyzed with respect to Grüneisen parameter using the following expression,

$$\gamma = \frac{B_0}{\omega}\frac{d\omega}{dP} \quad (2)$$

where ω is the mode frequency and "P" is the applied pressure. The bulk modulus B_0 is taken as 230 GPa[39]. Table 3 gives the experimental and theoretical frequencies with appropriate uncertainties at ambient pressure, pressure coefficients, and Grüneisen parameters of different phonon modes of α-Fe_2O_3 pseudocubic crystals. The experimental frequency of the Raman-active modes obtained from the present study agrees well with the previously reported values found in the literature as displayed in Table 4. Moreover, the experimental Grüneisen parameters coincide with those reported in the literature for bulk α-Fe_2O_3, which indicates the lack of influence of the low dimensionality in the HP dependence of Raman-active modes.

Symmetry	Experimental			Theoretical Simulation		
	$\omega_0(cm^{-1})$	$d\omega/dP$ $\left(cm^{-1}/GPa\right)$	γ	$\omega_0(cm^{-1})$	$d\omega/dP$ $\left(cm^{-1}/GPa\right)$	γ
A_{1g}^1	225.0(3)	0.79(3)	0.80(4)	204.9(5)	1.07(4)	1.20(5)
E_g^1	244.3(4)	1.00(3)	0.94(4)	213.3(12)	1.21(10)	1.30(11)
E_g^2	290.43(12)	0.878(11)	0.70(2)	267.9(9)	1.35(8)	1.30(7)
E_g^3	295.6(2)	2.160(19)	1.68(4)	275.1(6)	2.26(6)	1.88(7)
E_g^4	409.0(5)	3.22(4)	1.81(5)	371.3(5)	2.48(4)	1.53(4)
A_{1g}^2	498.9(6)	3.75(5)	1.72(4)	447.6(4)	4.35(3)	2.23(5)
E_g^5	611.2(8)	4.64(6)	1.74(4)	577.7(8)	5.22(7)	2.07(5)

Table 3: Pressure coefficients and Grüneisen parameters of all Raman-active modes of high index facets bounded α-Fe_2O_3 pseudocubic crystals at ambient pressure, obtained experimentally and also from theoretical simulations (Numbers within parentheses are estimated uncertainties or errors).

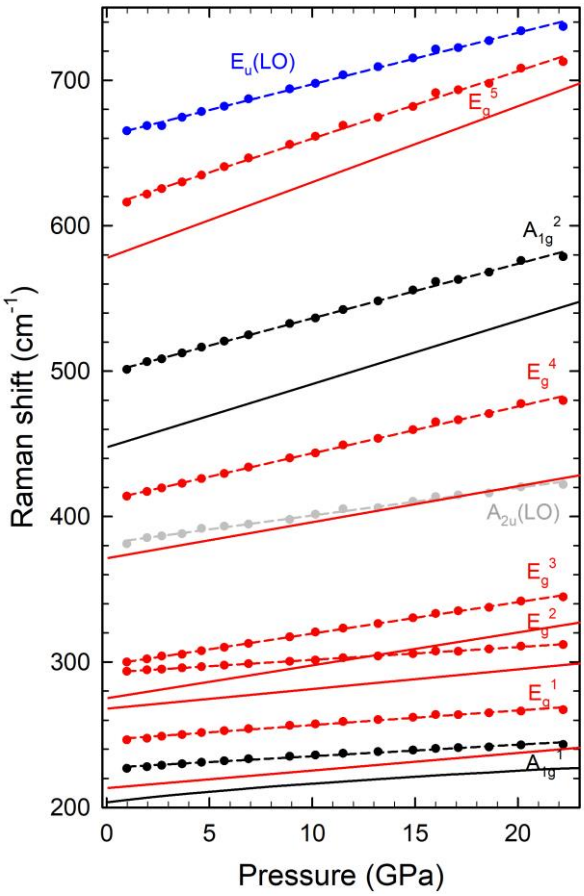

Figure 6: Theoretical simulations of pressure-dependent Raman shifts of high index facets bounded α-Fe_2O_3 pseudocubic crystals. Dotted lines represent the linear fit to the experimental data (solid spheres) and the solid lines represent the theoretical simulations.

In the present investigation on α-Fe_2O_3 pseudocubic crystals, the two additional features that appeared in the HP Raman measurements could not be assigned to any Raman-active modes, whose relative intensities are found to have increased with applied pressure. The influence of incident laser power on these Raman bands are further investigated by varying the power of the laser source at ambient conditions (Figure 7). The lack of influence of the incident laser intensity on these Raman features revealed that they are not related to 2^{nd}-order peaks, i. e. they do not correspond to the presence of traces of any other elements or impurities in the sample. In bulk samples, literature reported the presence of a peak at around 660 cm^{-1} that does not belong to any of the Raman-active modes. This peak is ascribed to $E_u(LO)$ mode, which is infrared-active by group theory. The activation of this mode in the Raman spectra of α-Fe_2O_3 pseudocubic crystals is associated with a strong Raman resonance on the surface, whose symmetry may not be completed, or structural defects induced by stress. Thus, the Raman feature appeared at 661 cm^{-1} is located at the same frequency as observed in the bulk samples which are tentatively assigned to $E_u(LO)$ mode as reported in the literature. However, this assignment is not clear since the $E_u(LO)$ and $A_{2u}(LO)$ fall into the same frequency at room conditions, making it impossible to distinguish their nature without the use of polarization or different HP

dependence. Regarding the polarization effect, we must account that the E_u (A_{2u}) modes are excited when the electric field is parallel (perpendicular) to the c-crystallographic axis. However, the powder nature of the sample makes it difficult to discern between both polarization geometries. Regarding the HP dependence, the theoretical simulations (Figure 8) showed that both these modes have the same behavior under compression, which annuls this strategy as well. On the other hand, the present sample showed an additional peak at 381 cm^{-1}, which has not been reported in the previous studies of bulk materials but appeared in the studies of nanocrystals [36,40,41]. This additional mode has been tentatively assigned to $A_{2u}(LO)$ infrared mode that is just as in the case of $E_u(LO)$ mode, has been activated by Raman by breaking up of the selection rules. However, the assignment of this mode showed a discrepancy with the frequency at the ambient conditions at which this mode is expected[36]. In literature, the emission spectroscopy has revealed a shift in frequency of $A_{2u}(LO)$ mode as an effect of the particle shape as a function of the excitation wavelength[42]. Thus, these infrared-active modes may be activated by the lack of a complete symmetry on the surface because, in nanoparticles, the surface-volume ratio is higher than that of the bulk samples. This may also be attributed to the presence of other phases of iron oxide (impurities) in the sample, but the Rietveld refinement carried out on the XRD pattern (Figure 2) revealed the absence of any other oxide phases of iron within the detection limit of the technique. In this case, the presence of Fe_3O_4 (magnetite) would also explain the appearance of a peak at 661 cm^{-1} but not the peak at 387 cm^{-1}. Moreover, in the study of the dehydration of FeOOH (mineral called goethite) by increasing the temperature to form α-Fe_2O_3, the formation of Fe_3O_4 (magnetite) as an intermediate has been proposed in the literature[43,44] which is later refused by De-Faria D. L. A. et al[45]. In a later publication, the authors heated a goethite sample to obtain α-Fe_2O_3 and the Raman scattering measurement of the resulting α-Fe_2O_3 had reported the presence of the same peaks as observed in the present work. Thus, the peak at around 657 cm^{-1} and a shoulder at a lower frequency than the peak at 409 cm^{-1} are detected, which may explain the feature given in our study at 381 cm^{-1}. They proposed the formation of defects as responsible for the appearance of these peaks and this may explain the increase in the intensity of these Raman features along with the applied pressure. The geometry and structural ordering of α-Fe_2O_3 pseudocubic crystals may be affected by the application of pressure generating defects, and geometrical distortions of the structure.

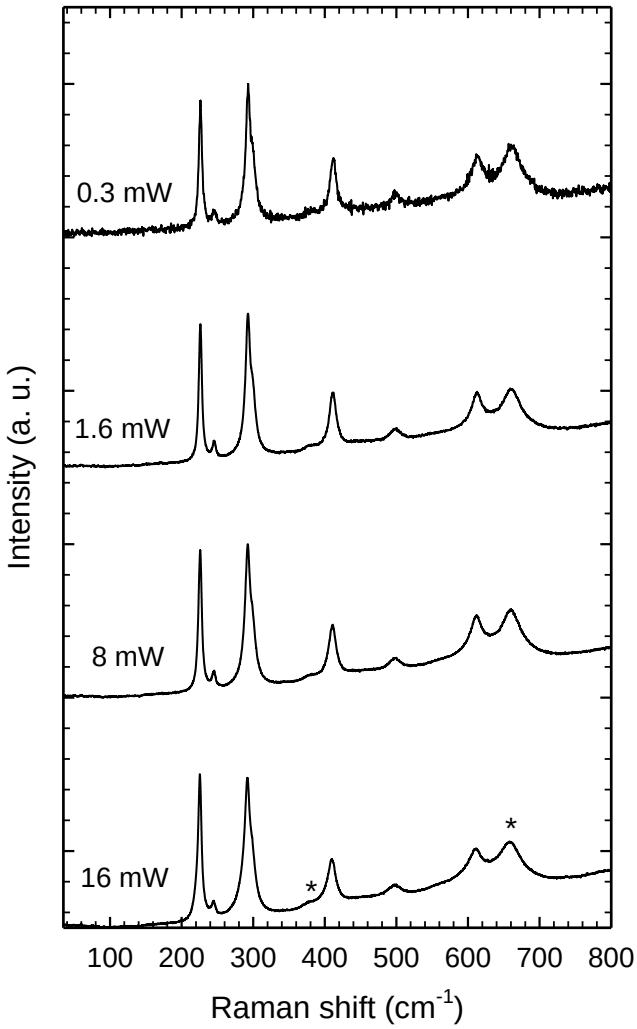

Figure 7: Raman spectra of high index facets bounded α-Fe_2O_3 pseudocubic crystals as a function of incident laser power. The two unexpected Raman features are indicated by asterisks.

	Present work (experimental)		Shim et al.[25]		Massey et al.[46]		Beattie et al.[47]
Mode symmetry	$\omega_0(cm^{-1})$	γ_0	$\omega_0(cm^{-1})$	γ_0	$\omega_0(cm^{-1})$	γ_0	$\omega_0(cm^{-1})$
$\mathbf{A_{1g}^1}$	225.0(3)	0.80(4)	224	0.76(10)	228	0.7(1)	226
$\mathbf{E_g^1}$	244.3(4)	0.94(4)	243	0.97(13)	246	1.1(1)	245
$\mathbf{E_g^2}$	290.43(12)	0.70(2)	290	0.45(6)	294	0.6(1)	293
$\mathbf{E_g^3}$	295.6(2)	1.68(4)	297	1.57(20)	300	1.8(1)	298
$\mathbf{E_g^4}$	409.0(5)	1.81(5)	408	1.31(16)	412	1.7(1)	413
$\mathbf{A_{1g}^2}$	498.9(6)	1.72(4)	496	1.27(16)	496	1.7(1)	500
$\mathbf{E_g^5}$	611.2(8)	1.74(4)	609	1.34(17)	614	2.0(2)	612

Table 4: Comparison of phonon frequencies and their mode Grüneisen parameters at ambient conditions obtained from this work with the values reported in the literature.

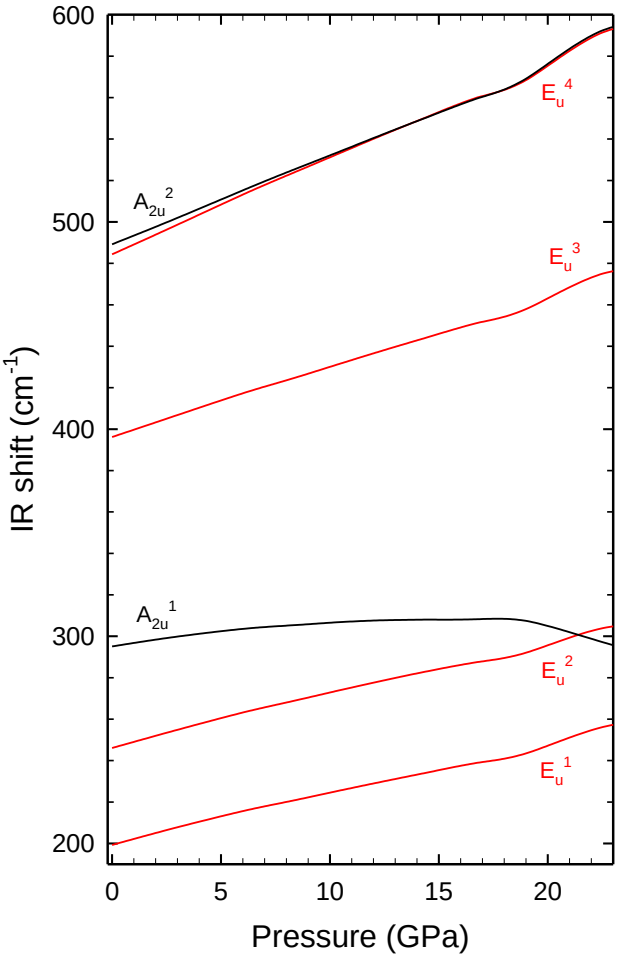

Figure 8: HP dependence of the frequency of the IR-active modes obtained by *ab-initio* theoretical calculations.

Conclusions

The solvo-hydrothermally synthesized high index facets {012}, {01$\bar{4}$}, and {$\bar{2}$10} bounded α-Fe_2O_3 pseudocubic crystals are investigated by Raman scattering measurements under high pressure (1-22.2 GPa) and the results are compared with the data derived from the *ab initio* calculations. All the Raman-active modes predicted by the group theory are observed experimentally under the whole pressure range, showing an agreement with the behavior of those simulated theoretically. No pressure-induced phase transition is observed within the investigated pressure range, which coincides with the strong stability of this compound as in bulk. In addition to the Raman-active modes, two additional Raman features are also detected. The influence of the laser excitation power is also investigated which evidenced that these peaks cannot be assigned to 2nd order Raman features. The comparison of these modes with the previous results found in the literature reveals that these additional features can be assigned to LO infrared-active modes, which might have been activated in the Raman spectra of α-Fe_2O_3 pseudocubic crystals by the breaking up of selection

rules, but the slight discrepancy in the frequency of A_{2u}(LO) mode is made with the formation of structural defects or distortions in the geometry, a more plausible explanation. This result exhibits a strong dependence on the geometry and the low dimensionality in the appearance of these unexpected peaks.

Acknowledgements

Neravathu G. Divya acknowledges DST FIST for FESEM analysis, Department of Physics, Cochin University of Science and Technology, Kerala, India. The author also acknowledges the Sophisticated Test and Instrumentation Centre (STIC), Kochi, India, for Rietveld Refinement measurements. This work is partly supported by Spanish MINECO under the projects MAT2016-75586-C4-2/3-P, FIS2017-83295-P, and MALTA Consolider Team project (RED2018-102612-T), and also by Generalitat Valenciana under project PROMETEO/2018/123-EFIMAT. JAS acknowledges the Ramón y Cajal program for funding supports through RYC-2015-17482 and VM to the Juan de la Cierva program through FJCI-2016-27921.

Data availability statements

The data that support the findings of this study are available from the corresponding author upon reasonable request.

References

[1] Machala L, Tuček J and Zbořil R 2011 Polymorphous transformations of nanometric iron(III) oxide: A review *Chem. Mater.* **23** 3255–72

[2] Tuček J, Machala L, Ono S, Namai A, Yoshikiyo M, Imoto K, Tokoro H, Ohkoshi S I and Zbořil R 2015 Zeta-Fe_2O_3 - A new stable polymorph in iron(III) oxide family *Sci. Rep.* **5** 1–19

[3] Zhan Y, Shen L, Xu C, Zhao W, Cao Y and Jiang L 2018 MOF-derived porous Fe_2O_3 with controllable shapes and improved catalytic activities in H_2S selective oxidation *CrystEngComm* **20** 3449–54

[4] Janghorban A M B H K, Hashemi B and Janghorban K 2016 α-Fe_2O_3 based nanomaterials as gas sensors *J. Mater. Sci. Mater. Electron.* **27** 3109–44

[5] Ranjithkumar V, Sangeetha S and Vairam S 2014 Synthesis of magnetic activated carbon/ α-Fe_2O_3 nanocomposite and its application in the removal of acid yellow 17 dye from water

J. Hazard. Mater. **273** 127–35

[6] Imran M, Shaik A H, Ansari A R, Aziz A, Hussain S, Fadil Abouatiaa A F, Khan A and Chandan M R 2018 Synthesis of highly stable γ-Fe_2O_3 ferrofluid dispersed in liquid paraffin, motor oil and sunflower oil for heat transfer applications *RSC Adv.* **8** 13970–75

[7] Shinde S S, Bansode R A, Bhosale C H and Rajpure K Y 2011 Physical properties of hematite α-Fe_2O_3 thin films: Application to photoelectrochemical solar cells *J. Semicond.* **32** 013001-08

[8] Lin Y M, Abel P R, Heller A and Mullins C B 2011 α-Fe_2O_3 nanorods as anode material for lithium ion batteries *J. Phys. Chem. Lett.* **2** 2885–91

[9] Neravathu D, Paloly A R, Sajan P, Satheesh M and Bushiri M J 2020 Hybrid nanomaterial of $ZnFe_2O_4$/α-Fe_2O_3 implanted graphene for electrochemical glucose sensing application *Diam. Relat. Mater.* **106** 107852-63

[10] Arun T, Prabakaran K, Udayabhaskar R, Mangalaraja R V, Akbari-Fakhrabadia A, 2019 Carbon decorated octahedral shaped Fe_3O_4 and α-Fe_2O_3 magnetic hybrid nanomaterials for next generation supercapacitor applications *Appl Surf Sci* **485** 147-157

[11] Sans J A, Monteseguro V, Garbarino G, Gich M, Cerantola V, Cuartero V, Monte M, Irifune T, Muñoz A and Popescu C 2018 Stability and nature of the volume collapse of ε-Fe_2O_3 under extreme conditions *Nat. Commun.* **9** 4554–65

[12] Liu R, Zhang Z, Liu Q, Zhu X, Yan Z, and Chen W 2015 Surface-dependent magnetic behavior of α-Fe_2O_3 quasi-cubes induced by Mg^{2+} ions CrystEngComm **17** 7107-12

[13] Wang L, Tang Y, Wang L, Zhu H, Meng X, Chen Y, Sun Y, Yang X J and Wan P 2015 Fast conversion of redox couple on $Ni(OH)_2$/C nanocomposite electrode for high-performance nonenzymatic glucose sensor *J. Solid State Electrochem.* **19** 851–60

[14] Wang F, Qin X F, Meng Y F, Guo Z L, Yang L X and Ming Y F 2013 Hydrothermal synthesis and characterization of α-Fe_2O_3 nanoparticles *Mater. Sci. Semicond. Process.* **16** 802–06

[15] Almeida T P, Fay M W, Hansen T W, Zhu Y and Brown P D 2014 Insights from in situ and environmental TEM on the oriented attachment of α-Fe_2O_3 nanoparticles during α-Fe_2O_3 nanorod formation *CrystEngComm* **16** 1540–46

[16] Raja K, Jaculine M M, Jose M, Verma S, Prince A A M, Ilangovan K, Sethusankar K and Das S J 2015 Sol-gel synthesis and characterization of α-Fe_2O_3 nanoparticles *Superlattices Microstruct.* **86** 306–12

[17] Shafi K V P M, Ulman A, Yan X, Yang N, Estourne C, White H, Rafailovich 2001 Sonochemical Synthesis of Functionalized Amorphous Iron Oxide Nanoparticles 5093–97

[18] Liu R, Jiang Z, Liu Q, Zhu X, Liu L, Ni L and Shen C 2015 Novel red blood cell shaped α-Fe_2O_3 microstructures and FeO(OH) nanorods as high capacity supercapacitors *RSC Adv.* **5** 91127–33

[19] Yin J, Yu Z, Gao F, Wang J, Pang H and Lu Q 2010 Low-Symmetry Iron Oxide Nanocrystals Bound by High-Index Facets *Angew. Chem. Int. Ed.* **49** 6328–32

[20] Wu W, Jiang C Z and Roy V A L 2016 Designed synthesis and surface engineering strategies of magnetic iron oxide nanoparticles for biomedical applications *Nanoscale* **8** 19421–74

[21] Zhan Y, Shen L, Xu C, Zhao W, Cao Y and Jiang L 2018 MOF-derived porous Fe_2O_3 with controllable shapes and improved catalytic activities in H_2S selective oxidation *CrystEngComm* 20, 3449-54.

[22] Liu R, Jiang Y, Lu Q, Du W and Gao F 2013 Al^{3+}-controlled synthesis and magnetic property of α-Fe_2O_3 nanoplates *CrystEngComm* **15** 443–46

[23] Zhao J, Chen H S, Matras-Postolek K and Yang P 2015 Morphology evolution of α-Fe_2O_3 controlled via incorporation of alkaline earth metal ions *CrystEngComm* **17** 7175–81

[24] Divya N G and Bushiri M J 2019 High index facet bounded α-Fe_2O_3 pseudocubic nanocrystals with enhanced electrochemical properties: Zn^{2+} ion assisted solvo-hydrothermal synthesis *CrystEngComm* **21** 1378–88

[25] Shim S H and Duffy T S 2001 Raman spectroscopy of Fe_2O_3 to 62 GPa *Am. Mineral.* **87** 318–26

[26] Liu H, Caldwell W A, Benedetti L R, Panero W and Jeanloz R 2003 Static compression of α-Fe_2O_3: Linear incompressibility of lattice parameters and high-pressure transformations *Phys. Chem. Miner*. **30** 582–88

[27] Ono S, Kikegawa T and Ohishi Y 2004 High-pressure phase transition of hematite, Fe_2O_3 *J. Phys. Chem. Solids* **65** 1527–30

[28] Hohenberg P and Kohn W 1964 Inhomogeneous Electron Gas Phys. Rev. **136**, B864-71

[29] Blöchl P E 1994 Projector augmented-wave method *Phys. Rev. B* **50** 17953–79

[30] Dudarev S L, Botton G, Savrasov S Y, Humphreys C J and Sutton A P 1998 Electron-energy-loss spectra and the structural stability of nickel oxide: An LSDA+U study *Phys. Rev. B* **57** 1505–9

[31] Mujica A, Rubio A, Muñoz A and Needs R J 2003 High-pressure phases of group-IV, III-V, and II-VI compounds *Rev. Mod. Phys.* **75** 863–12

[32] Togo A and Tanaka I 2015 First principles phonon calculations in materials science *Scr. Mater*. **108** 1–5

[33] Parlinski K, Li Z Q and Kawazoe Y 1997 First-principles determination of the soft mode in cubic ZrO_2 *Phys. Rev. Lett.* **78** 4063–76

[34] Schouwink P, Dubrovinsky L, Glazyrin K, Merlini M, Hanfland M, Pippinger T and Miletich R 2011 High-pressure structural behavior of α-Fe_2O_3 studied by single-crystal x-ray diffraction and synchrotron radiation up to 25 GPa *Am. Mineral.* **96** 1781–86

[35] Lemine O M, Bououdina M, Sajieddine M, Al-Saie A M, Shafi M, Khatab A, Al-Hilali M and Henini M 2011 Synthesis, structural, magnetic and optical properties of nanocrystalline $ZnFe_2O_4$ *Phys. B* **406** 1989–94

[36] Jubb A M and Allen H C 2010 Vibrational spectroscopic characterization of hematite, maghemite, and magnetite thin films produced by vapor deposition *ACS Appl. Mater.*

Interfaces **2** 2804–12

[37] Lassoued A, Dkhil B, Gadri A and Ammar S 2001 Control of the shape and size of iron oxide (α-Fe_2O_3) nanoparticles synthesized through the chemical precipitation method *Results Phys* **7** 3007–15

[38] Porto S P S and Krishnan R S 1967 Raman effect of corundum *J. Chem. Phys.* **47** 1009–12

[39] Olsen J S, Cousins C S G, Gerward L, Jhans H and Sheldon B J 1991 A study of the crystal structure of Fe_2O_3 in the pressure range up to 65 GPa using synchrotron radiation *Phys. Scr.* **43** 327–30

[40] Serna C J, Rendon J L and Iglesias J E 1982 Crystal-chemical study of layered ($Al_2Li(OH)6$)+X-.nH_2O. *Clays Clay Miner.* **30** 180–84

[41] Onari S, Arai T and Kudo K 1977 Infrared lattice vibrations and dielectric dispersion in α-Fe_2O_3 *Phys. Rev. B* **16** 1717–21

[42] Rendon J L and Serna C J 1981 IR spectra of powder hematite: effects of particle size and shape *Clay Miner.* **16** 375–81

[43] Dekkers M J 1990 Magnetic properties of natural goethite–III. Magnetic behaviour and properties of minerals originating from goethite dehydration during thermal demagnetization *Geophys. J. Int.* **103** 233–50

[44] Özdemir Ö and Dunlop D J 2000 Intermediate magnetite formation during dehydration of goethite *Earth Planet. Sci. Lett.* **177** 59–67

[45] de Faria D L A and Lopes F N 2007 Heated goethite and natural hematite: Can Raman spectroscopy be used to differentiate them? *Vib. Spectrosc.* **45** 117–21

[46] Massey M J, Baier U, Merlin R and Weber W H 1990 Effects of pressure and isotopic substitution on the Raman spectrum of +-Fe_2O_3: Identification of two-magnon scattering *Phys. Rev. B* **41** 7822–27

[47] Beattie I R and Gilson T R 1970 The Single-crystal Raman Spectra of Nearly Opaque Materials. Iron(II) Oxide and Chromium(III) Oxide *J. Chem. SOC. A,* 980-986